THE JOURNAL OF PHYSICAL CHEMISTRY C
A JOURNAL OF THE AMERICAN CHEMICAL SOCIETY

pubs.acs.org/JPCC

Article

Interfacial Thermal Transport and Electrical Performances of Supercapacitors with Graphene/Carbon Nanotube Composite Electrodes

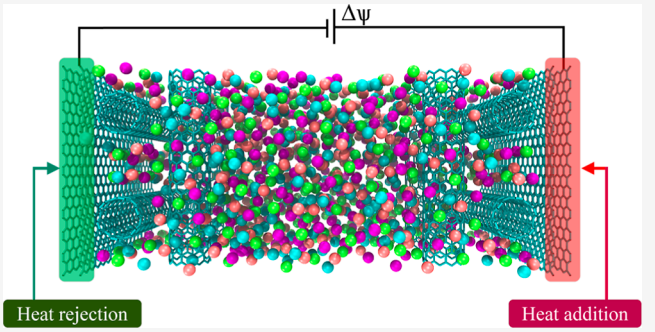
Sobin Alosious,* Shern R. Tee, and Debra J. Searles*

Cite This: *J. Phys. Chem. C* 2024, 128, 2190−2204

Read Online

ACCESS | Metrics & More | Article Recommendations | Supporting Information

ABSTRACT: Advanced supercapacitors have great potential to transform how we store and utilize energy, leading to more efficient and sustainable energy systems. This study reveals the structural features influencing the interfacial thermal transport and electrical performances of supercapacitors using the constant potential and constant charge molecular dynamics simulation techniques. Thermal and electrical properties were calculated for graphene/carbon nanotube (CNT) composite electrodes and ionic liquid electrolytes with different nanotube diameters, numbers, layers, and alignments of the nanotubes. The effect of the application of a constant potential on the Kapitza resistance is determined for the first time. The vertically aligned CNT structures exhibited higher electrical performance, while the horizontal arrangement showed better thermal performance. Optimum electrode configurations were identified by considering thermal and electrical performances along with other design factors, such as structural stability, ease of manufacturing, and scalability. After considering all these factors, the horizontally stacked multilayer CNT arrangement emerged as the optimal electrode structure. The insights gained from this study aid in comprehending the effects of variations in the electrode structure, thereby enabling efficient supercapacitor electrode design.



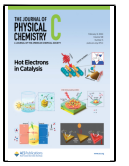
Downloaded via UNIV OF NOTRE DAME on July 11, 2026 at 17:16:27 (UTC).
See https://pubs.acs.org/sharingguidelines for options on how to legitimately share published articles.

INTRODUCTION

Double-layer supercapacitors, also known as ultracapacitors, are energy storage devices that deliver high power and rapid charge−discharge cycles. Compared to batteries, they generally have faster charge and discharge rates and longer lifetimes and can operate at a broader range of temperatures. However, their energy density tends to be much lower, making research into new supercapacitor materials and structures of great importance. Supercapacitors have numerous applications in various industries, including transportation[1] (e.g., electric buses and trains), aerospace[2] (e.g., satellites), renewable energy[3] (e.g., wind turbines and solar cells), and consumer electronics[4] (e.g., smartphones and laptops). They are beneficial for applications that require frequent cycles or continuous operation, where traditional batteries may fail. As technology advances, the demand for supercapacitors is expected to increase due to their unique advantages over battery technologies.

The heat generated within the supercapacitor and its temperature rise quickly when a large number of supercapacitors are packed in small volumes to attain high energy density. The operating temperature of a supercapacitor has a significant influence on its performance characteristics[5] as temperature deviations strongly influence the properties of electrolytes (such as viscosity, the solubility of the salt in solvents, ionic conductivity, thermal stability, decomposition, and solvent evaporation). Other issues associated with temperature deviations include self-discharge and a reduction in capacitance and lifespan.[6,7] The heat generation in a supercapacitor is primarily due to irreversible Joule heating, which happens as the charging or discharging current passes through the equivalent series resistance (ESR) of the supercapacitor. The ESR includes contributions from the resistance at the interface between the electrode and the current collectors, the electrode and electrolyte resistances, and resistance as ions diffuse through electrode pores or through the separator.[8,9] Apart from the irreversible Joule heating losses, reversible heat generation caused by the entropic effect occurs while charging or discharging a supercapacitor. Unlike irreversible Joule heating, the reversible heat generation rate is positive during charging and negative during discharging.[10,11] It is essential to dissipate the heat generated in a supercapacitor to maintain the system at a rated temperature, and

Received: November 3, 2023
Revised: December 18, 2023
Accepted: January 2, 2024
Published: January 27, 2024



ACS Publications
© 2024 American Chemical Society

https://doi.org/10.1021/acs.jpcc.3c07299
J. Phys. Chem. C 2024, 128, 2190−2204

the interfaces in supercapacitors are the principal barriers to heat dissipation. The electrolyte−electrode interface exhibits the highest heat barrier due to insufficient contact at the solid−liquid interface.

Thermal management of supercapacitors and batteries has been carried out using different cooling techniques;[12] however, the interfacial thermal resistance (ITR), despite being the principal barrier to heat dissipation, has received less attention. Thus, extensive knowledge of the molecular-level interfacial thermal transport mechanisms in supercapacitors is critical for optimizing heat dissipation, safety, and stability. ITR, or Kapitza resistance (R_K),[13] measures the thermal flow resistance of an interface. In other words, when there is a heat transfer across an interface between two different materials, a temperature discontinuity arises due to the thermal resistance at that interface. This thermal resistance, due to the disparity in the electronic and vibrational characteristics of the two materials in contact, is called ITR and is given by

$$R_K = \frac{\Delta T}{J_q} \tag{1}$$

where J_q is the heat flux across the interface and ΔT is the temperature difference between the materials in contact. Computational studies have proven valuable in developing an understanding of the fundamental mechanism of interfacial thermal transport between solid−fluid interfaces,[14−18] including graphene−ionic liquid (IL) interfaces which are more relevant for supercapacitor thermal transport.[19] Qian et al.[20] investigated the ITR and structure at the interface between graphene and the IL and observed that the molecular orientation of ions near the solid surface dominates the degree of heat transfer at the imidazolium-based IL-graphene interface. The increased wettability at the interface can enable thermal transport by improving the contact between the IL and graphene, with the alignment of the imidazole ring linearly related to the ITR. Finally, they have also predicted the lower limit of the ITR (~6 m^2 K GW^{-1}) between the IL and graphene when the imidazole ring is parallel to the graphene sheet.

Improving a supercapacitor's performance primarily involves maximizing its energy density and capacitance, which can be accomplished through developing new electrode and electrolyte materials.[21] Carbon-based electrodes are widely used in supercapacitors due to their advantages, such as a large surface area, good flexibility, high electrical conductivity, good chemical and thermal stability, and a broad potential window. Carbon-based electrode materials in the literature include activated carbon, carbide-derived carbon, carbon monoliths, and graphene−carbon nanotube (CNT) composites.[22−26] Péan et al.[27] studied the charging of electrified nanoporous carbide-derived carbon (CDC) electrodes with the help of molecular dynamics (MD) simulations. Their study revealed that the charging process occurs diffusively, originating from the interface between the CDC and BMI-PF_6 electrolyte and gradually penetrating the bulk of the electrode. Similar results were obtained by Maji et al.[28] who carried out experimental and computational studies of an aqueous electrolyte with CDC electrolytes, showing how diffusion rates differ in regions of the supercapacitor. In both cases, the CDC exhibited significant heterogeneities at the nanoscale, comprising a complex pore network with varying pore sizes, setting it apart from other structures, such as CNTs and slit pores. Their findings indicated that certain parts of the CDC will start charging earlier than others, despite being located deeper within the electrode due to the intricate nature of porous networks.

When analyzing the performance of supercapacitors using computer simulation techniques, CNT-graphene electrodes have advantages in that they provide many of the features of realistic systems such as pore networks, different degrees of curvature, and a distribution of pore sizes while being highly reproducible. Composite electrodes that combine CNTs and graphene possess sufficient intercalation of CNTs between graphene layers, allowing for ample void space for ion diffusion throughout the electrode. Several studies have been conducted to understand the mechanism of CNT−graphene-based electrodes.[29−31] McDaniel[32] has developed a modified constant potential MD algorithm to enable highly efficient simulations of supercapacitors and predicted the relation between the capacitance and structure of five different graphene/CNT composite electrodes with an IL electrolyte. They observed that the graphene/CNT contact points behave as "hot spots" with dramatically increased charge separation and reported a 40% increase in the differential capacitance of a specific electrode model as a result of nanoconfinement effects. Their findings showed how the electrode/electrolyte interface for nanoporous carbon electrodes might exhibit substantial heterogeneity in the ion concentration profiles and electrostatic interactions.

The constant potential MD method has been widely used to model the electrodes due to its better accuracy for simulations of electrochemical interfaces. Merlet et al.[33] compared the constant charge method (CCM) and constant potential method (CPM) in modeling supercapacitors based on IL electrolytes and graphite electrodes and observed a change in the fluid structure and time scales over which relaxation phenomena happen, especially for nanoporous supercapacitors. The difference in the structure of the electrolyte increases with an increase in the electrode charge, which may lead to a shift in the thermodynamic properties of the system. They showed that the results obtained from the constant charge method do not accurately represent the system's properties. Furthermore, they found that the heat generation due to the Joule effect during the formation of an electric current follows Ohm's law for the CPM, while the CCM displays an unphysical temperature jump. However, the direct use of CPM for thermal analysis of electrodes was not possible since electrode particle positions remained immobilized at all times in the implementation of CPM.

In this paper, we investigate the interfacial thermal transport and electrical properties of a graphene−IL supercapacitor using nonequilibrium MD simulations. The ITR calculated using the constant potential and constant charge methods is compared for the first time. In addition, we have modeled different types of graphene/CNT composite electrodes by varying geometrical parameters such as diameter, number, layers, and alignment of CNTs. The electrical and thermal performances of each electrode morphology were investigated based on different parameters. Optimum electrode structures with high specific capacitance, improved heat transfer properties, and consideration of several design parameters were identified. In what follows, we present a summary of the modeling, the methodology adopted for the simulation, discussions about the obtained results, and, finally, some concluding remarks.

https://doi.org/10.1021/acs.jpcc.3c07299
J. Phys. Chem. C 2024, 128, 2190−2204

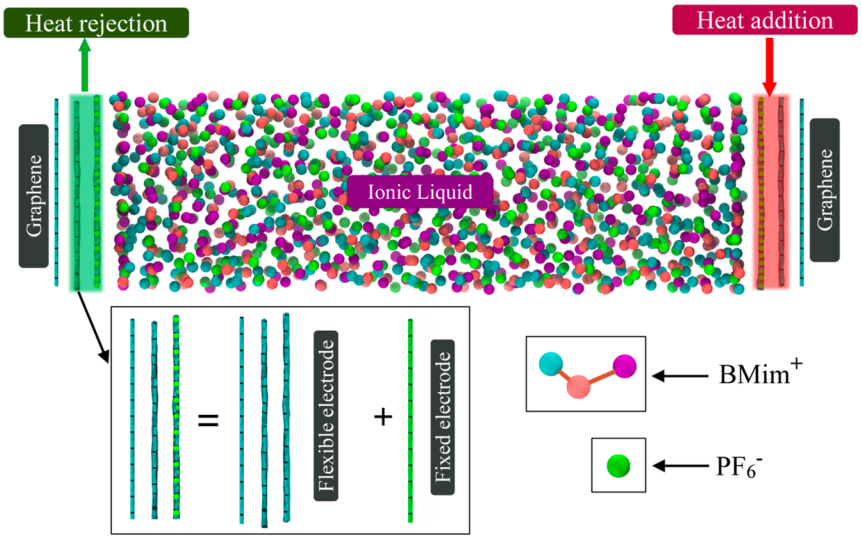


Figure 1. Schematic depiction of the graphene-IL supercapacitor model. The electrode is divided into a flexible and fixed graphene layer for thermal and electrical analyses.

METHODOLOGY

CPM Overview. Supercapacitors are often modeled in MD by assigning a uniform and constant charge to all particles in an electrode and observing how the electrolyte's structure and dynamics change with the magnitude of the applied uniform charge. Such "constant charge" simulations can give reasonable results for the structural properties of the electrolyte near a charged electrode but fail in more complicated situations, such as for nanostructured electrodes, high voltages, or complex electrolytes like ILs.[33,34] By contrast, in the CPM for MD simulations, conductive electrodes are modeled by dynamically updating their partial charges to achieve electrostatic equipotential across each electrode.[35] If the N_e electrode particles are immobile, the partial charges can be efficiently calculated via one additional electrostatic potential evaluation per MD time step, whereas mobile electrodes require an additional $N_e \times N_e$ matrix inversion or an iterative minimization process each time step. We refer the reader to other publications for the mathematical and implementation details.[36] CPM MD adds accuracy to electrode−electrolyte simulations by including electrolyte forces due to the induced polarization of the electrode. In particular, CPM MD can realistically simulate nanostructured electrodes that cannot be approximated as uniformly charged planes. Since electrode charges respond dynamically to the electrolyte configuration, charging and discharging dynamics can also be simulated with CPM MD, unlike in constant charge simulations, resulting in physically meaningful equivalent circuit parameters.[37]

Evaluation of the ITR Using Constant Potential and Constant Charge Methods. In the first part of our study, we compare the CPM to constant charge simulations for evaluating the ITR and using it to directly assess the performance of different supercapacitor nanostructures. We assess the effect of different electrode charging procedures in a model supercapacitor (Figure 1), consisting of planar graphene electrodes with a coarse-grained IL electrolyte, before analyzing more complicated graphene−CNT morphologies in the next part of our study.

In our model supercapacitor, each electrode is made of three layers of graphene with each layer having different dynamics. For each electrode, the layer furthest from the electrolyte is a base layer and remains immobile, or nonthermalized, throughout the simulation (but still exerts forces on all other electrolyte and electrode atoms), while the next two layers are thermalized and move over the course of the simulation. All the flexible layers are separately modeled using an optimized Tersoff potential,[38] while the non-Coulombic interactions between flexible graphene layers and the electrolyte are modeled using Lennard-Jones (LJ) potentials. In addition, the outermost fixed graphene layers on both ends interact with the electrolyte and flexible layers using the corresponding LJ parameters.

The Coulombic interaction between the electrode and electrolyte is then modeled by adding a lattice of charge sites to the proximal electrode layer closest to the electrolyte, with the same initial positions as the carbon atoms. To enable thermal measurements, we introduce a novel, computationally efficient method where the graphene carbon atoms are fully mobile but are associated with charge sites that remain fixed to make the CPM calculations faster. Since the electrodes must be fixed when using the CPM, an additional layer of graphene (a dummy electrode) is placed exactly at the initial position of the actual electrode by overlapping its coordinates. Thus, the electrodes are divided into two parts: the flexible and fixed electrodes. Of these electrodes, one graphene electrode is modeled with the optimized Tersoff potential, making it a flexible electrode. Another graphene layer is kept immobile, overlapping the flexible layer, and taken as the fixed electrode. All interactions (LJ and Coulombic) between the flexible and fixed electrodes are completely disabled to ensure that the overlap of the electrodes has no impact on the simulation. The interactions between the electrode and electrolyte then consist of two parts. The flexible electrode is responsible for the LJ interactions, whereas the fixed electrode takes care of the short-range Coulombic interactions between the electrode and electrolyte. The CPM is now applied to the fixed electrode, while the Tersoff potential is applied to the flexible electrode. This is appropriate in the cases we consider here where the electrode atoms do not move far from their original sites (less than ~0.24 Å). We use charge updating for only the graphene layer closest to the IL as we have previously found that—due to the electrodes being overall conductive—charge updates to

https://doi.org/10.1021/acs.jpcc.3c07299
J. Phys. Chem. C 2024, 128, 2190−2204

the underlying layers have negligible effect on the ions' local electric field and thus on the simulation dynamics.[39] To see the effect of this approach, we treat the charge sites using three different methods to identify the effects of various approximations:

- In Method 1, which is our new approach, the charge sites are kept spatially immobile, and their charges are updated using CPM MD with matrix multiplication (which is computationally efficient but requires immobile charge sites), but the carbon atoms are mobile.
- In Method 2, the charge sites are kept spatially immobile, and each site is given a uniform charge that also stays constant over time (positive for the anode and negative for the cathode). The total electrode charge is set to the average value obtained from the Method 1 simulations, but constant potential is not used to update individual electrode charges. The carbon atoms are mobile.
- In Method 3, uniform, constant charges are still used for the charge sites, but they are now made mobile and move in tandem with the carbon atom positions used for non-Coulombic interactions, whereas the previous two methods use static charge sites and mobile non-Coulombic sites.

Thus, the difference between results from Method 1 and Method 2 is due to changing from CPM MD to constant charge MD, while the difference between results from Method 2 and Method 3 is due to changing from immobile to thermally mobile fixed-charge sites.

MD Simulation Details. The supercapacitor considered for the initial study consists of an IL electrolyte confined between planar graphene electrodes, as schematically depicted in Figure 1. Both electrodes consist of three layers of graphene sheets separated by a distance of 3.35 Å.[40] The intermolecular interactions of the IL are via a coarse-grained model of 1-*n*-butyl-3-methylimidazolium hexafluorophosphate [$BMim^+$]-[PF_6^-] IL developed by Roy and Maroncelli.[41] In this model, the cations are represented as three-site molecules that are kept rigid using the SHAKE[42] algorithm, while the anions are represented as single particles. Several bulk characteristics, including molar volume, isothermal compressibility, viscosity, and diffusion, can be reliably predicted by using this IL model. We note that IL models with finer details are increasingly prevalent in literature, especially polarizable models,[43−45] which capture important nonadditive behavior and their effects on local dynamics, and we hope to study the accuracy increases available from atomistic and polarizable models in future work after having established the basic correctness of our methods.

Periodic boundary conditions are imposed in the x and y directions with dimensions of 32.2 and 34.4 Å, respectively. The distance between the proximal electrodes is kept at 109.75 Å to maintain the bulk density of the IL (1.267 g cm^{-3}) at the center bulk portion of the cell. MD simulation models of supercapacitors with similar electrode−electrolyte combinations, force fields, and dimensions have been used in previous works.[39,46] The long-range electrostatic forces are estimated by employing the particle−particle−particle−mesh[47] solver with an accuracy of 10^{-8}, and the Ewald summation technique with an extended volume ratio of 3.0 is used to adjust the z-direction confinement.[48] The pairwise interactions between all the atoms are calculated using LJ and Coulombic potentials with a cutoff distance of 16 Å. The Lorentz−Berthelot mixing rules are used to obtain the LJ parameters for the cross-terms. The equations of motion of all of the particles are integrated using a velocity-Verlet algorithm with a time step of 1 fs. The LAMMPS (large-scale atomic/molecular massively parallel simulator) package[49] is used for conducting all the MD simulations, and the ELECTRODE[35] package is utilized for the CPM. The visualization and rendering of models are carried out using visual MD[50] and the open visualization tool.[51]

The initial modeling of the simulation setup is carried out by following similar steps as in our previous work, and the same model is used in this study as well.[39] The system is equilibrated, and the electrode distance is adjusted to obtain a bulk density of 1.267 g cm^{-3} at the center of the IL channel. Charge sites are then added to the system as needed (for Methods 1 and 2), and the entire system is equilibrated under a canonical (NVT) ensemble at 400 K for a time period of 5.0 ns after energy minimization. During this process, a thermostat is applied to the flexible electrode and the IL, and one of the three charge methods in the previous section is used. To examine how potential differences affect ITR, nine different potential differences (0.0, 0.5, 1.0, 1.5, 2.0, 2.5, 3.0, 4.0, and 5.0 V) are utilized. As used in previous studies,[34] the electrode charges are modeled as Gaussian distributions with a width parameter η = 1.979 Å.[39] After this equilibration process, the system will be at a constant temperature, and the average charge on the electrodes will converge to constant values (for Method 1 simulations). After the equilibration process, NEMD simulations are carried out to calculate the ITR at the electrode−electrolyte interface. To generate a temperature gradient across the system, heat is added and removed from both ends of the system using a Langevin thermostat with a damping parameter of 100 fs.[52] A linear temperature gradient along the z-direction is generated by providing two different temperatures (350 and 450 K) on both ends of the system, as shown in Figure 1. This process is continued for 5.0 ns until the system reaches a steady state, at which point the net heat flux across the system converges to a constant value. The ITR can be calculated using eq 1. The temperature drop at the interface is measured from the temperature profile, and the heat flux is calculated using the energy added and subtracted from the thermostat per unit surface area per unit time. Another set of simulations is conducted to study the change in ITR during the charging process. To calculate the ITR variation during the charging process, the constant potential method is turned off during the initial equilibration and heat addition/removal processes and later turned on during the production run. Thus, the charging process begins at the production run, which allows us to calculate the ITR during specific intervals of the charging process.

Graphene/CNT Composite Electrodes. The second part of this study involves analyzing the electrical and thermal performances of different graphene/CNT composite electrode morphologies. Graphene/CNT composite electrodes with 14 different combinations are used in this study. The electrode arrangements can be classified into four categories depending upon the CNT diameter, number of CNTs, number of layers of CNT, and arrangement of CNTs (vertical/horizontal). A typical electrode in this study comprises a graphene layer with Lx = Ly = 40 Å and different CNT combinations. All of the electrode structures and their denotations mentioned throughout this paper are shown in Figure 2. The effect of the CNT

https://doi.org/10.1021/acs.jpcc.3c07299
J. Phys. Chem. C 2024, 128, 2190−2204

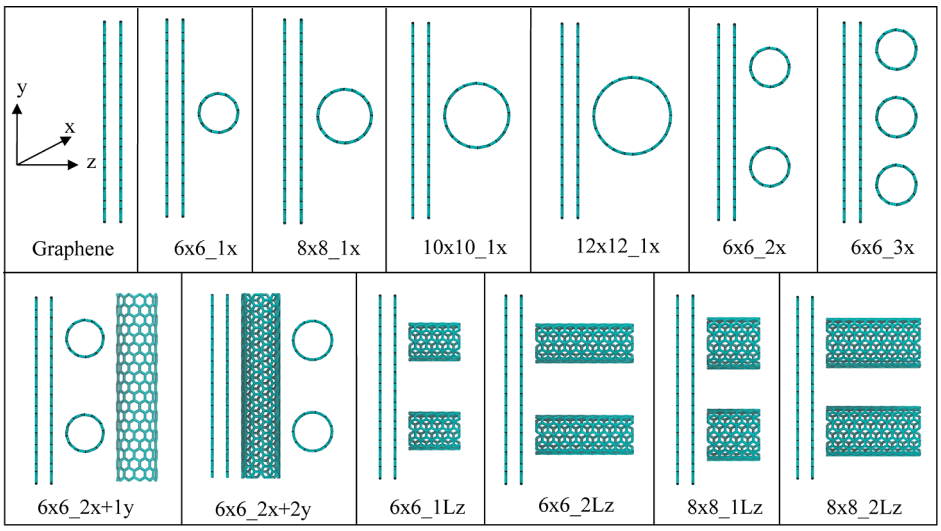


Figure 2. Different morphologies of graphene/CNT composite electrodes considered here are classified based on the diameter, number, layers, and alignment of CNTs. The notation used for electrodes is indicated and is based on the characteristics of CNTs.

diameter is studied by using four different diameters varying from 8.25 to 16.5 Å [(6,6), (8,8), (10,10), and (12,12)]. A CNT of 40 Å length is placed at the center of the graphene layer with its axis parallel to the x direction. The graphene layers are periodic in the x and y directions, whereas the CNT is periodic in the x direction. Similarly, the number of CNTs on the electrode varies from 1 to 3 using (6,6) CNTs placed equidistant and parallel to the graphene layer. The complexity and porosity of the electrode are again increased by adding another layer of CNT on top of the first layer. Two such models are prepared by varying the number of CNTs on the second layer. The second layer is also a (6,6) CNT with a length of 40 Å and its axis parallel to the y direction. For initialization, the electrodes in this study are positioned with a packing distance of 3.35 Å between graphene−CNT and CNT−CNT. All of the individual atoms of CNTs are tethered to their initial positions using a weak harmonic spring potential, ensuring the structure of the electrodes remains the same. Finally, four additional sets of electrodes are modeled by placing the CNTs perpendicular to the graphene. Four CNTs are positioned with their axes perpendicular to the graphene plane (parallel to the z-direction). Varying the length and diameter of the CNTs results in four distinct configurations utilizing a combination of (6,6) and (8,8) CNTs with lengths of 10 and 20 Å. The supercapacitor models are generated by filling $[BMim^+][PF_6^-]$ IL between the symmetric anode and cathode configurations corresponding to each electrode. The distance between the anode and cathode in each system is adjusted to maintain a constant pressure and temperature. This is achieved by applying a force equivalent to 1 bar of pressure on top of one electrode (the other electrode is kept fixed) and allowing it to equilibrate until the pressure stabilizes. Once the system is stabilized, the average distance between the cathode and anode is calculated and set as the distance between electrodes. This process is repeated for all systems to ensure proper electrolyte filling inside the pores of the graphene/CNT composite electrodes.

During each production run, the electrodes are modeled using the constant potential method with flexible carbon atoms (using the same modified Tersoff potential as above) and immobile charge sites (Method 1). Again, the outermost graphene layers on both sides are always kept immobile. A schematic diagram of the supercapacitor used in this study, featuring a graphene/CNT composite electrode and an IL electrolyte, is shown in Figure 3. This particular system

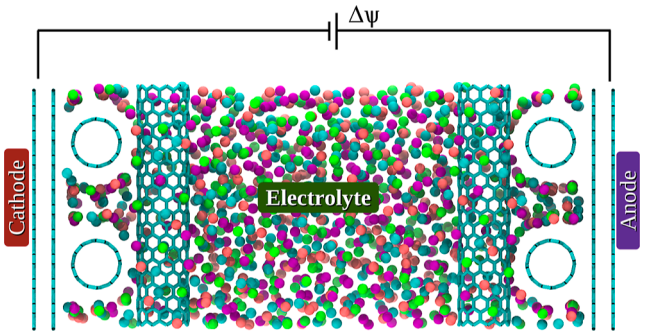


Figure 3. Schematic diagram of the two-layer ($6 \times 6_2x + 2y$) supercapacitor model. The pores of the electrode are filled by the ions by placing the system under 1 bar of pressure at 400 K.

consists of two layers of (6,6) CNTs stacked on top of each other to form a two-layer CNT arrangement. The potential difference across the electrodes is varied from 0.0 to 4.0 V to study supercapacitors' thermal and electrical properties under varying potential differences. Finally, the NEMD simulation steps mentioned in the previous section are followed for the thermal analysis.

RESULTS AND DISCUSSION

Comparison of Constant Potential and Constant Charge Methods. The interfacial thermal transport is investigated in a graphene−IL supercapacitor by conducting nonequilibrium MD simulations, where a temperature gradient along the z direction is generated by adding and removing heat from the anode and cathode, respectively. The temperature profile across the system after reaching a steady-state heat flux is illustrated in Figure 4. A linear temperature gradient is apparent across the IL channel. However, there is a temperature discontinuity at the interface between the electrode and electrolyte. This discontinuity or jump in

https://doi.org/10.1021/acs.jpcc.3c07299
J. Phys. Chem. C 2024, 128, 2190−2204

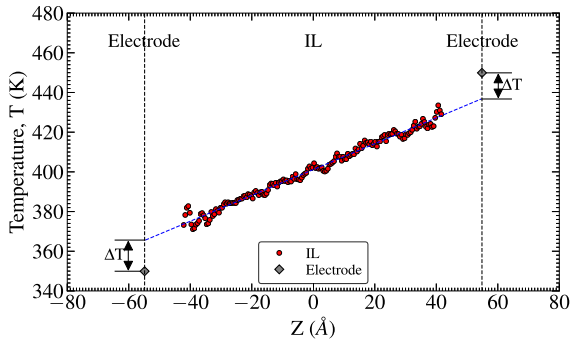


Figure 4. Temperature profile along the confinement direction of the graphene supercapacitor.

temperature, ΔT, is due to the ITR between graphene and the IL, adversely affecting interfacial heat transport. The temperature jump ΔT can be directly determined from the temperature profile, and the heat flux J_q can be calculated by extracting the cumulative energy added and removed from the thermostat. With knowledge of both the heat flux and temperature jump, the ITR (ITR) can be directly calculated using eq 1.

Figure 5 compares the ITR as a function of the potential difference, calculated using the three methods described above.

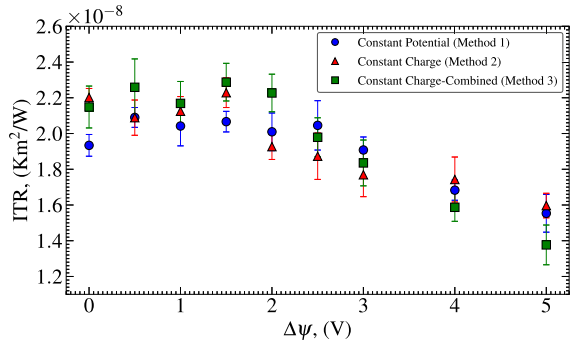


Figure 5. Comparison of the ITR as a function of the potential difference for the graphene supercapacitor calculated using the three methods [Method 1—constant potential, Method 2—constant charge, and Method 3—constant charge (combined)] . The error bars are the standard errors in the ITR from five independent simulations with different initial configurations.

They are found to have overlapping error bars (shown as one standard error in the mean of five independent simulations), and no systematic differences can be seen between any of the modeling methods used. All three methods produced similar qualitative trends of the ITR being constant between 0 and 2 V and decreasing with an increasing potential difference after that. Although the three methods compared give similar results, their required computational costs differ greatly. By comparing the CPU hours per nanosecond simulation, it was found that Method 2 (constant charge) demonstrates a reduction of roughly 27% in CPU hours per nanosecond compared to Method 1 (constant potential). Similarly, Method 3 (constant charge-combined) exhibits a substantial decrease, approximately 45%, in CPU hours per nanosecond compared to that of Method 1.

Furthermore, as shown in Figure 5, the ITR appears to be relatively insensitive to potential differences at lower values and decreases as the potential difference increases. In a computational study by Alexeev et al.,[17] it was reported that the ITR strongly depends on the height of the first water density peak at a graphene−water interface. However, for the graphene−IL interface, the first density peak height alone does not fully explain the trend of ITR variation with increasing potential difference. Alosious et al.[53] later reported that the area density factor (the ratio of the number of molecules in a fluid slab adjacent to the interface to the interface's surface area) is a primary factor in determining the ITR at a CNT−water interface as it accounts for curvature. Similarly, we consider the total mass in a slab of the IL adjacent to the graphene electrode (for planar interfaces, the surface area will be the same in all cases). The slab's thickness is chosen to accommodate the first few density peaks, unlike Alexeev et al.[17] who consider only the first density peak. Analysis of the normalized slab mass revealed that the trend in slab mass variation with an increasing potential difference is inversely related to the ITR's dependence on potential difference (see Supporting Information for slab mass analysis). We propose that this is because a higher slab mass enhances heat transfer at the interface, reducing the ITR. This result suggests that the interfacial thermal transport in graphene−IL interfaces is not just a function of the first density peak but is also influenced by the successive peaks, especially for a higher electrode charge density. As the potential difference increases, the surface charge density on the electrode surface increases, resulting in additional Coulombic interactions between the electrode and electrolyte in addition to van der Waals interactions. The influence of this electrostatic interaction is limited not only to the first layer but also to the successive layers of the IL. Furthermore, it has been observed that the ITR exhibits variations between the anode and cathode interfaces, which can be attributed to the asymmetrical ion structure near the interface when a potential difference is introduced.

Although the CCM has been deemed adequate for studying interfacial thermal transport in supercapacitors, a CPM is necessary to comprehend the variations in ITR during the charging and discharging processes. The utilization of CPM allows us to observe the changes in the ITR during the charging process, as shown in Figure 6. Since the surface charge density of the electrode influences the interfacial thermal transport, the ITR is expected to decrease with an increase in potential difference. Ideally, the ITR is calculated using the time-averaged (entire production run) heat flux and temperature jump; however, only short intervals are available for computing the averaged value during the charging process,

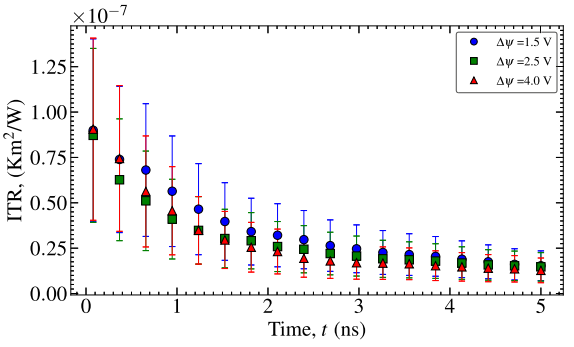


Figure 6. Variation in the ITR during the charging process of the graphene supercapacitor using CPM (Method 1). The error bars are the standard error in the mean of five independent simulations.

https://doi.org/10.1021/acs.jpcc.3c07299
J. Phys. Chem. C 2024, 128, 2190−2204

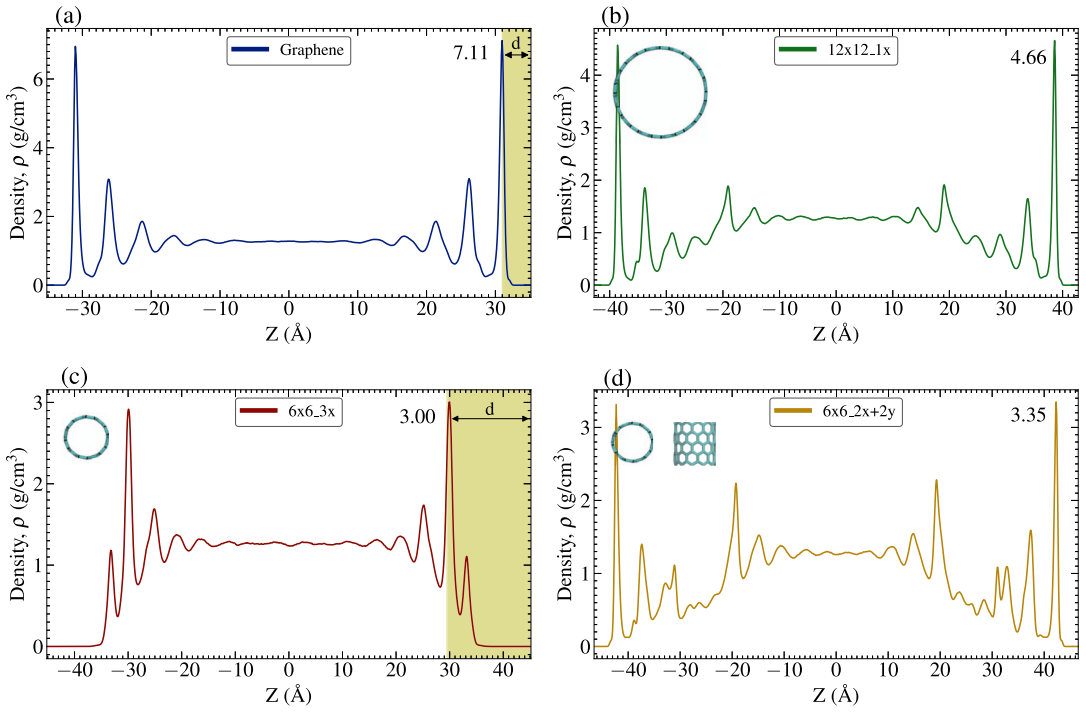


Figure 7. Density profiles of the IL liquid for a few selected systems. (a) Planar graphene. (b) 12 × 12_1*x* model. (c) 6 × 6_3*x* model. (d) 6 × 6_2*x* + 2*y* model. The height of the first liquid density peak is marked near the peak. The distance from the graphene layer to the first density peak is denoted as "*d*". The positions of CNTs in the *z*-axis are shown using the structure of the CNT.

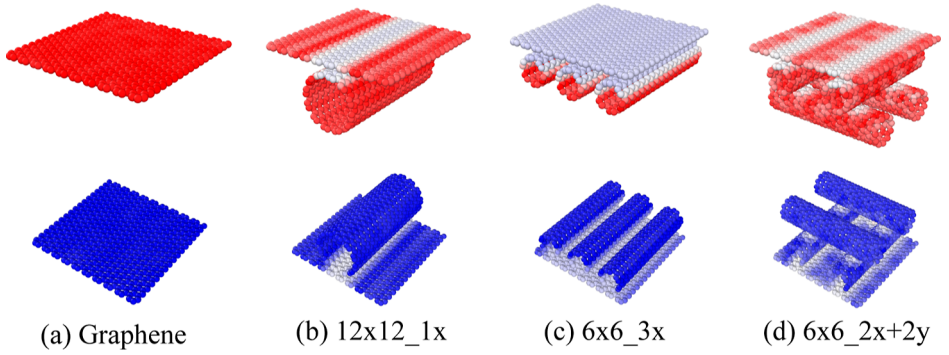


Figure 8. Surface charge distribution on the electrode induced by the cations and anions averaged over the entire simulation time using CPM with a potential difference of 4 V. (a) Planar graphene. (b) 12 × 12_1*x* model. (c) 6 × 6_3*x* model. (d) 6 × 6_2*x* + 2*y* model.

leading to large statistical uncertainties in the ITR. Consequently, a qualitative inference is favored over quantitative results in this particular case. It is critical to consider that the ITR and heat transfer vary throughout the charging and discharging process when designing and modeling supercapacitor interfaces and estimating heat dissipation.

Graphene/CNT Composite Electrodes. The third part of this study focuses on examining a supercapacitor's electrical and thermal characteristics by employing diverse combinations of graphene/CNT composite electrodes. MD simulations were carried out using Method 1, as discussed in the Methodology section. Figure 7 displays the density profiles of the IL for a select set of systems. A typical density profile of an IL confined between uncharged planar graphene sheets is shown in Figure 7a. The height of the first density peak is about 6.5 g cm^{-3}, and interfacial layering can be seen up to 25 Å from the graphene surface. When a single CNT of diameter 16.5 Å (12,12) is attached horizontally to the graphene, the structure of the IL near the electrode is changed and is shown in Figure 7b. The first density peak is reduced to 5 g cm^{-3} due to the reduced contact between the IL and graphene in the presence of the CNT. Moreover, an additional density peak adjacent to the CNT emerges, and the interfacial layering region extends to 40 Å. Figure 7c illustrates the IL structure when three (6,6) CNTs are stacked horizontally on the graphene. The density peak is shifted toward the bulk portion, indicating that the contact between the IL and graphene is shadowed by the CNTs. The distance between graphene and the first density peak, *d*, increased from 4 to 16 Å compared to that of the planar graphene electrode. In addition to the diminished contact between graphene and the IL, the height of the density peak is also reduced compared to that of planar graphene, which shows poor solid−fluid wetting despite having an additional surface area. Similarly, Figure 7d shows the structure of the IL for a two-layer system. Here also, we can see a reduction in the maximum density peak and large layering region due to the filling of the IL inside the porous structure. However,

https://doi.org/10.1021/acs.jpcc.3c07299
J. Phys. Chem. C 2024, 128, 2190−2204

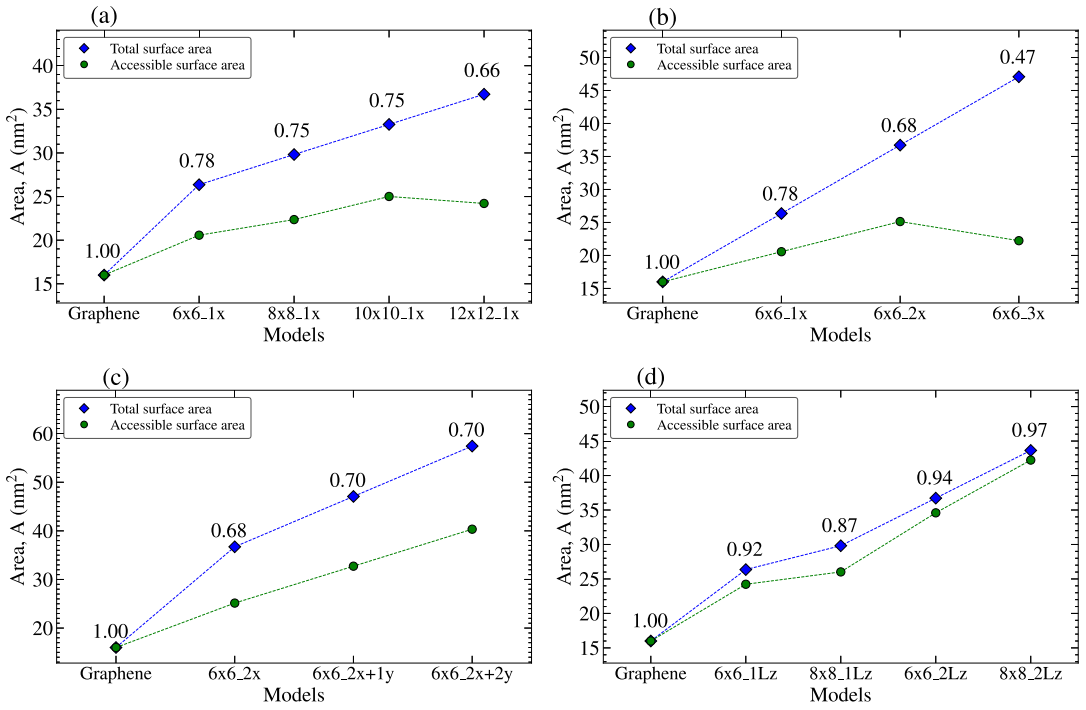


Figure 9. Comparison of the ASA and TSA for all the electrodes classified based on the (a) CNT diameter, (b) number of CNTs, (c) number of CNT layers, and (d) vertical arrangement of CNTs. The ratio between ASA and TSA for all of the electrodes is also denoted.

compared to planar graphene, a higher number of density peaks can be seen, suggesting an enhancement in interfacial wetting. Similar structural patterns can also be observed in vertical arrangements and other horizontal systems.

From the above discussion, it is clear that the structure of the IL and the contact between the electrode and electrolyte vary depending on the morphology of the electrode. In particular, the electrode morphology is likely to change the local ionic ordering significantly, which promises to be a rewarding area for future study. For simplicity, we generated surface charge contours for the electrodes and analyzed these to understand the distribution of induced charge on the electrodes. Figure 8 shows the surface charge distribution on the electrode induced by the cations and anions averaged over the entire simulation time (using CPM). The surface charge distribution of all of the electrodes can be found in the Supporting Information. The induced charge on each atom is measured and averaged over the whole simulation time used to plot the charge contour. Blue and red represent positive and negative charges, respectively, while white indicates zero charge. For a planar graphene electrode, the time-average surface charge density is equally distributed over the entire graphene surface (without any white spots), as illustrated in Figure 8a. This shows a very efficient contact between the electrode and electrolyte. However, for a graphene/CNT composite electrode, some areas with almost zero charge density (depicted as white spots in Figure 8b,c) suggest that there is a portion of the electrode (the contact point of graphene and CNT) that is inaccessible to the IL. For instance, a large area with zero charge is visible for the three-graphene/CNT electrode system (Figure 8c), indicating an inefficient contact between the electrode and electrolyte. Since the electrode is periodic in the x and y directions, the number of CNTs effectively means the distance between the CNTs. Here, the entire graphene surface and about half of the CNT surface are inaccessible to the IL, resulting in an inefficient electrode−electrolyte contact. Similarly, Figure 8d shows the charge contour for a two-layer CNT electrode system, in which the white regions are visible on different electrode positions. This particular stacking arrangement mimics a porous electrode structure, with IL filling the pores. The charge is induced on the electrode structure, except for the contact points between graphene and CNTs. The surface charge density contours in Figure 8 provide a qualitative understanding of the interaction between the electrolyte and various electrode structures.

The addition of CNTs in different dimensions and arrangements increases the total surface area (TSA) of the electrode. However, it should be noted that an increase in the TSA does not necessarily equate to a proportional increase in the area that is accessible to the electrolyte as this is dependent on the electrode morphology. To assess the efficacy of each electrode, we calculated the accessible surface area (ASA) for all of the electrodes. The ASA is calculated using the "rolling ball" algorithm, which probes the surface and pores of the electrode with a sphere equivalent to the size of ions.[54] We selected a radius of 2.5 Å, which is comparable to the size of the PF_6^- anion. To establish whether a point is accessible or buried, all points are examined on the surfaces of nearby atoms. Finally, the ASA is calculated by multiplying all the accessible points by the surface area of each point. Also, the TSA is calculated by adding the surface area of graphene and the lateral surface area of CNTs. The horizontally aligned CNTs act as infinite cylinders due to their periodicity. Therefore, the IL cannot occupy the interior space of the CNTs. In contrast, the interior space of vertically aligned CNTs is available for the IL. Consequently, when calculating the ASA, the inner surface area is not considered for horizontally aligned CNTs, whereas it is taken into account for vertically aligned CNTs.

https://doi.org/10.1021/acs.jpcc.3c07299
J. Phys. Chem. C 2024, 128, 2190−2204

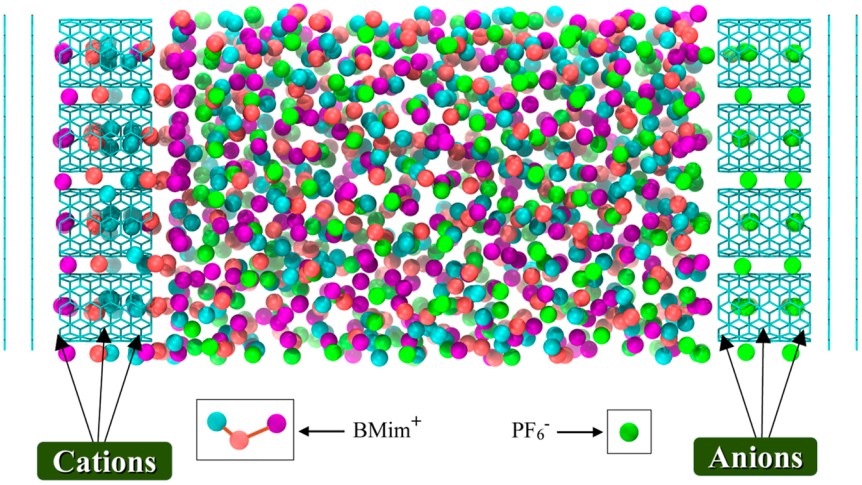


Figure 10. Schematic diagram of the closely packed vertical CNT electrode system. The selective entry of cations inside anode pores and anodes inside cathode pores under a 4.0 V potential difference is depicted.

Figure 9 compares the TSA with the ASA for all of the electrodes, and their ratio is also indicated. The TSA is always higher than the ASA as it represents the maximum available surface area. From here on, the comparison of different properties is classified into four categories based on the diameter, number, layer, and alignment of CNTs on graphene. An increase in the diameter of the CNT results in an increase in both TSA and ASA, and the ratio is about 0.79 for all four diameters, as depicted in Figure 9a. From Figure 9b, it is clear that adding two (6,6) CNTs in parallel increases the ASA, but adding one more CNT drastically reduces the ASA to 0.47 of the TSA, indicating that almost half of the electrode surface is inaccessible to the electrolyte. Therefore, increasing the number of CNTs or closely packing them will limit the filling of the pores by the electrolyte. On the other hand, Figure 9c shows that stacking more layers increases the ASA without compromising the ASA/TSA ratio. Stacking CNTs one above another can control the porosity of the electrode, thereby optimizing the electrode structure per requirement. Finally, the ASA for the vertical arrangement is illustrated in Figure 9d. Since the CNT is vertically positioned, the inside volume of the CNT is also accessible to the ions if the ion size is smaller than the CNT diameter. Also, there are no bulky contact points between graphene and CNTs, unlike in the horizontal arrangement. Therefore, the ASA/TSA ratio is higher for vertical than horizontal stacking.

Selective Ion Entry. When a CNT of sufficiently high diameter is oriented perpendicular to graphene, ions can penetrate inside it. It was found that for the (8,8) CNT, both the anion and cation can enter the CNT at zero potential difference. However, for the (6,6) CNT, the diameter is not big enough for the ions to enter inside at zero potential. Nevertheless, when a potential difference is applied across the supercapacitor, we found that cations and anions enter the CNTs connected to the anode and cathode. To better understand the dependence of CNT filling on potential difference, another electrode was modeled with 16 (6,6) CNTs vertically aligned, as illustrated in Figure 10. This closely packed arrangement ensures that the ions cannot pass through the gap between CNTs. This system is also equilibrated under 1 bar of pressure, similar to other models. When the potential difference is zero, none of the ions can enter the CNTs or the gap between CNTs. However, when a potential difference is applied, all of the anode CNTs are filled with cations and vice versa. Figure 10 shows that only the anions are inside the cathode CNTs and the cations are inside the anode CNTs. This way, we can completely separate the anions and cations and attach them to the cathode and anode. This mechanism can be achieved by choosing the correct CNT diameter, considering the size of the ions. Density profiles of both anions and cations, with and without applied potential, are provided separately in the Supporting Information. Even though a perfect double-layer (the ideal case for an EDLC supercapacitor) can be achieved on both electrodes, the specific capacitance of the supercapacitor cannot be improved due to ineffective contact between the electrode and electrolyte. Since the CNTs are tightly packed, the ASA for ions is much less, making this type of arrangement ineffective in improving the performance of a supercapacitor. Even though this electrode morphology is unsuitable for supercapacitors, this technique can be used in other applications, such as desalination and ion separation.[55] While this study utilizes a coarse-grained model of the IL instead of an atomistic one, it is expected that the same phenomenon will still be observed, despite a potentially different quantitative trend for the physical system.

Electrical Properties. One of the primary objectives of this work is to compare the electrical properties, such as the capacitance and energy density of the supercapacitor, by using different electrode morphologies. The double-layer capacitance of a supercapacitor primarily depends on the potential drop ($\Delta\psi = \psi^{\text{cathode}} - \psi^{\text{anode}}$) across the cell and the surface charge density (σ) of the electrode. The potential drop is considered the difference between the electrostatic potential drop in the charged capacitors and the discharged capacitors

$$\Delta\Delta\psi = \Delta\psi^{\text{charge}} - \Delta\psi^{\text{uncharge}} \tag{2}$$

whereas the surface charge density is the average surface charge on the electrode divided by the surface area of the electrode. The surface can be either the TSA or the ASA, and the following analyses consider the ASA for all of the calculations unless specified. Usually, capacitance can be classified into two categories: integral and differential capacitance. Integral capacitance is calculated by taking the ratio of the average charge density to the potential drop across the capacitor

https://doi.org/10.1021/acs.jpcc.3c07299
J. Phys. Chem. C 2024, 128, 2190−2204

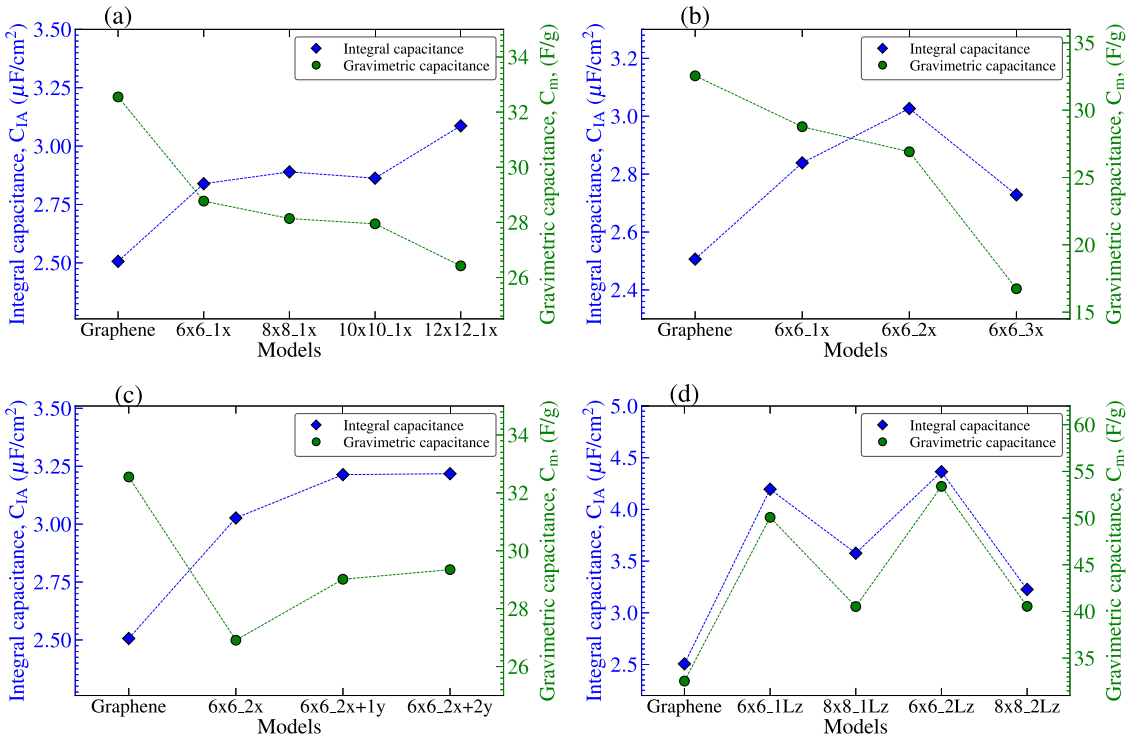


Figure 11. Integral capacitance, C_I (calculated based on the ASA), and gravimetric capacitance, C_m (calculated based on the TSA), for all the electrode models classified based on the (a) CNT diameter, (b) number of CNTs, (c) number of CNT layers, and (d) vertical arrangement of CNTs.

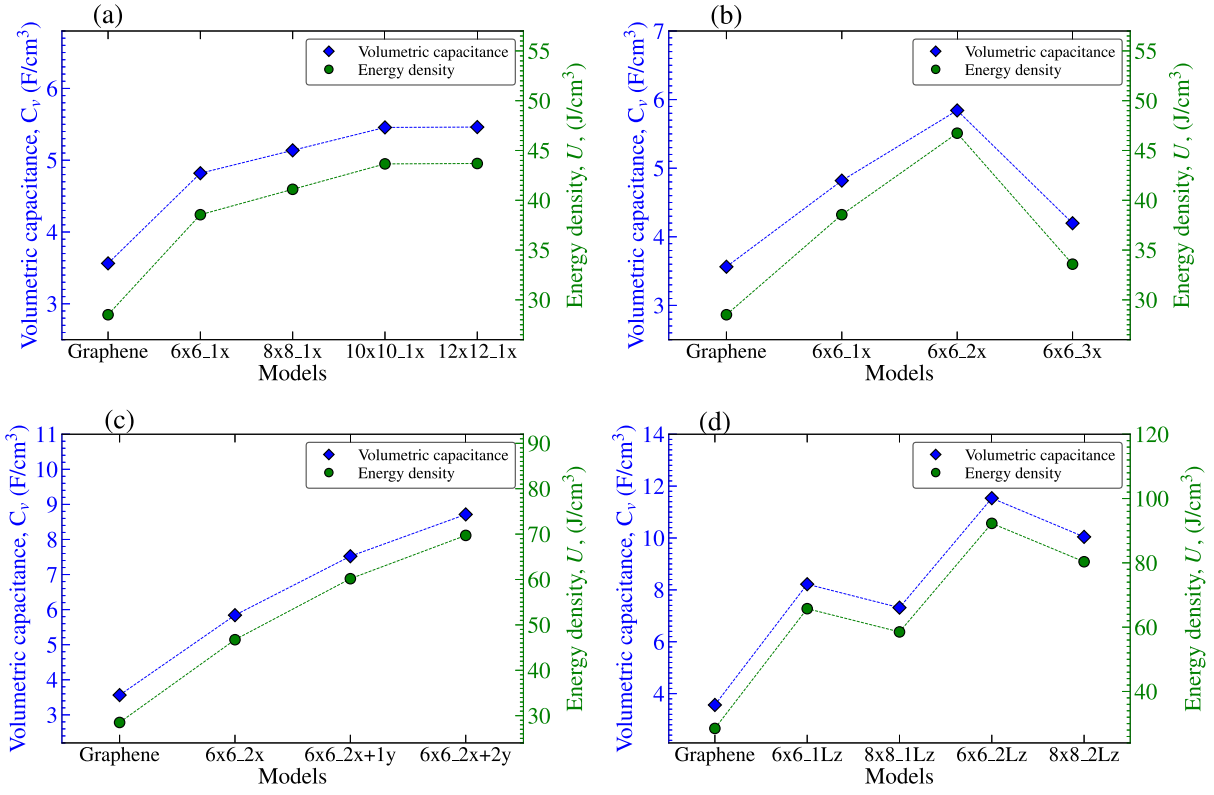


Figure 12. Volumetric capacitance, C_v, energy density, and U for all the electrode models classified based on the (a) CNT diameter, (b) number of CNTs, (c) number of CNT layers, and (d) vertical arrangement of CNTs.

$$C_I = \frac{|\sigma|}{\Delta\Delta\psi} \quad (3)$$

The differential capacitance from the rate of change of charge density as a function of the potential drop

https://doi.org/10.1021/acs.jpcc.3c07299
J. Phys. Chem. C 2024, 128, 2190−2204

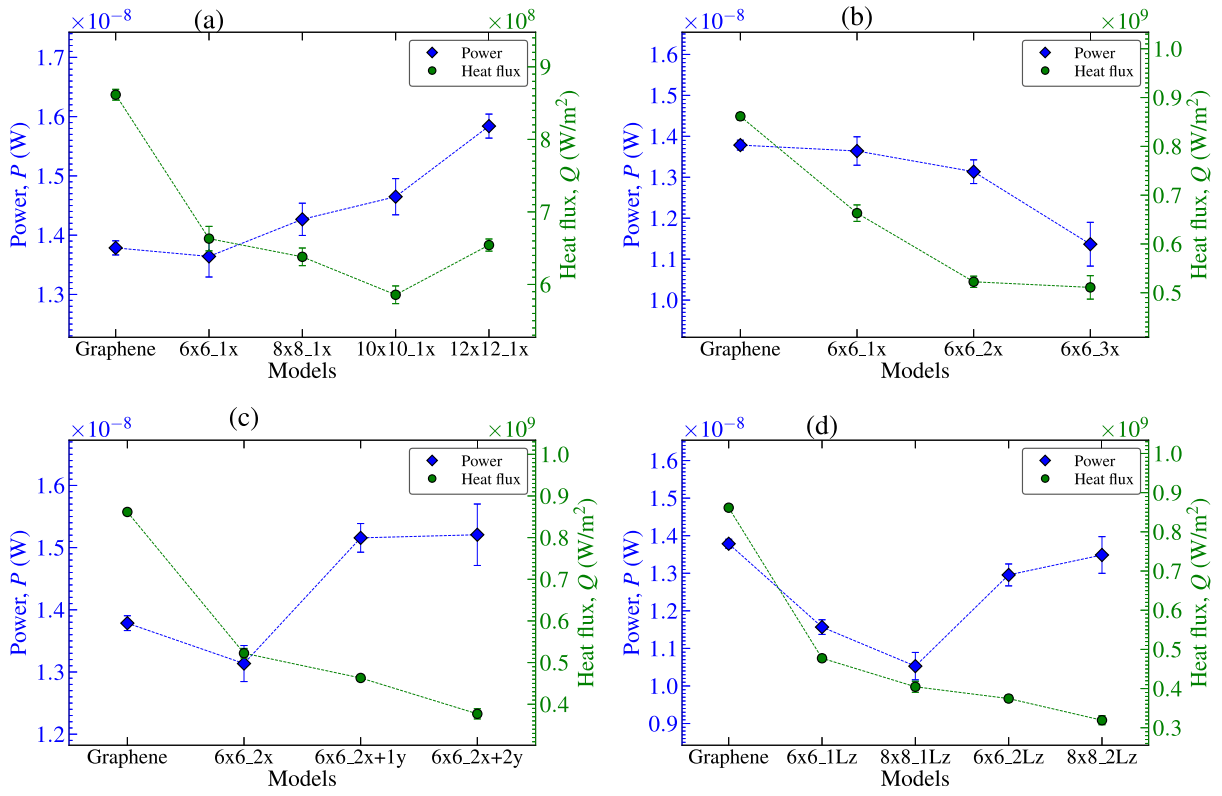


Figure 13. Thermal power output, P, and heat flux, Q, for all the electrode models classified based on the (a) CNT diameter, (b) number of CNTs, (c) number of CNT layers, and (d) vertical arrangement of CNTs.

$$C_D = \frac{d\sigma}{d\psi} \tag{4}$$

Since this study focuses on the overall electrical performance of the supercapacitor for different electrode structures, integral capacitance is used throughout this paper. Figure 11 shows the comparison of integral capacitance and gravimetric capacitance for different electrode structures, where the gravimetric capacitance is calculated from the total mass of carbon atoms in each electrode. Adding horizontal CNTs lowers the gravimetric capacitance compared to that of planar graphene, indicating a reduced contact efficiency between the electrode and electrolyte. The integral capacitance still increases with the addition of one- or two-CNT horizontal layers, showing that the overall performance still improves, but the three-CNT horizontal layer reduces both the integral and gravimetric capacitance, indicating that ions are obstructed by too many layers of closely packed CNTs. From Figure 11c, we can see that adding a second layer of CNT will modestly increase gravimetric and integral capacitances compared to those of a single layer of horizontal CNTs. The capacitance with vertically added CNTs is shown in Figure 11d, which shows overall higher gravimetric and integral capacitances compared to those of planar graphene. Indeed, the vertical arrangement of 6 × 6 CNTs of length 2 nm ($6 \times 6_2Lz$) has the highest capacitance value among all the electrodes studied.

Furthermore, we have computed the volumetric capacitance and energy density of the supercapacitor for all electrodes and illustrated them in Figure 12. The volumetric capacitance is given by

$$C_v = \frac{C}{V} \tag{5}$$

where C is the capacitance. The energy density is given by

$$U = \frac{C_I \cdot [\Delta\Delta\psi]^2}{2V} \tag{6}$$

where V is the volume of the supercapacitor and the capacitance is taken to be C_I. Here, the volume is calculated by considering the box size of each supercapacitor model. From Figure 12a, we can see that the volumetric capacitance and energy density increase with an increase in the diameter and converge above 10 × 10 CNT. This indicates that increasing the diameter after a particular value gives no advantage. When it comes to an increase in the number of CNTs, adding a third CNT or decreasing the distance between CNTs drastically lowers the volumetric capacitance and energy density, as depicted in Figure 12b. The electrode with a second CNT layer, however, enhances the volumetric capacitance and energy density. Additionally, for vertical systems, smaller CNT diameters and longer lengths lead to better performance. These findings suggest that vertical CNT stacking is superior to horizontal stacking since it provides the ions with better access to almost the entire CNT surface, resulting in improved electrical properties. However, the disadvantages of the vertical system are the difficulty in manufacturing such electrodes and their scalability. In contrast, for horizontal systems, the most effective electrode is the two-layer configuration, which is relatively easy to produce and can be scaled up by increasing the number of layers.

Thermal Properties. To ensure the maximum performance of the supercapacitor, it is crucial to maintain its temperature within a specified range. Efficient dissipation of heat generated within the supercapacitor is necessary to maintain the temperature. Hence, interfacial thermal transport,

https://doi.org/10.1021/acs.jpcc.3c07299
J. Phys. Chem. C 2024, 128, 2190−2204

which plays a significant role in heat dissipation, must be considered while designing the electrode. The ITR or Kapitza resistance is the primary parameter determining the heat transfer property of an interface.[56] However, in this study, the interface between the electrode and electrolyte cannot be defined due to the complexity of the electrode structure. Therefore, the heat transfer performance of each electrode is calculated based on the power and heat flux dissipated from each electrode. The power output is calculated by measuring the average cumulative energy added and removed from the thermostat and dividing by the simulation time. On the other hand, the heat flux is calculated by dividing the heat power output by the ASA of the electrode.

The heat flux and power output for all of the electrodes are illustrated in Figure 13. It is observed that the planar graphene electrode has the highest heat flux of all the electrodes. Here, the heat flux shows how effectively heat transfer takes place at the electrode. A higher heat flux value for graphene, and lower heat flux values when adding CNTs, indicates that adding CNTs will increase the interfacial resistance to heat flow as a result of worse contact between CNTs and electrolyte. However, the heat power output trend shows that, despite increasing the ITR, the total thermal energy dissipated still increases when CNTs are added due to the overall increase in the surface area. As depicted in Figure 13a, the power output increases with the diameter of the CNT, while heat flux decreases until 10 × 10, then slightly increases with a further diameter increase. From Figure 13b, it is clear that when the number of CNTs increases, the heat flux and power output decrease, indicating an unfavorable design for thermal aspects. This reduction can be attributed to the improper contact between the electrode and electrolyte, which leads to inefficient thermal transport. Interestingly, adding a second layer of CNTs improves heat transfer in addition to better electrical performance, as depicted in Figure 13c. Even though the ITR is reduced, adding CNTs increases the total surface available for heat transfer, resulting in a visible increase in power in most horizontal systems. Figure 13d shows that power and heat flux are lower in vertical systems than in graphene, indicating that the heat transfer efficiency is not advantageous for the vertical arrangement of CNTs. Furthermore, longer CNTs exhibit superior power dissipation compared with shorter ones.

To gain a deeper comprehension of the heat transfer mechanism at the electrode−electrolyte interface, we have also investigated the vibrational density of states (VDOS) of the IL and all of the electrodes. The calculation and results of the VDOS are described in the Supporting Information. The VDOS overlap between electrodes showed no significant change, suggesting that the vibrational coupling between the electrode and IL remains unaffected by changes in the electrode structure. Hence, the observed alteration in interfacial thermal transport due to the inclusion of CNTs cannot be attributed to changes in the vibrational spectrum, as noted in earlier studies.[17,57] Consequently, the change in interfacial thermal transport can be attributed to the electrolyte structure adjacent to the electrode interface. As discussed earlier, the height of the density peak or the mass of the electrolyte present near the electrode can be used to understand the variation in heat transfer with each electrode. From Figure 7, it is clear that the height of the first density peak is highest for graphene, indicating a higher wetting coefficient leading to lower thermal resistance. Therefore, the interfacial thermal transport between the electrode and electrolyte can be predicted by knowing how densely packed the ions are in and around the pores of the electrode.

Optimum Electrode Structure. Finally, we try to identify an electrode structure that maximizes both electrical and thermal performances based on volumetric capacitance and heat dissipation, respectively (Figure 14). Of all the electrode

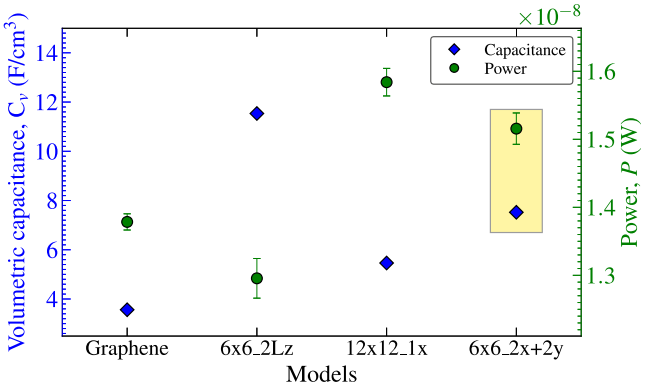


Figure 14. Volumetric capacitance, C_v, and thermal power output, P, compared for selected electrodes to quantify electrical and thermal performances with metrics included for graphene as a comparison point.

structures considered, the vertical arrangement of 6 × 6 CNTs with 2 nm length (6 × 6_2Lz) has the highest volumetric capacitance of approximately 13.6 F cm^{-3}, but its thermal performance is inferior to all other electrodes. Similarly, the single CNT system with a 12 × 12 chirality (12 × 12_1x) has the highest power output of approximately 1.58 × 10^{-8} W, but its electrical performance is the worst among the chosen electrodes. Therefore, it is clear that the electrode structure with the highest electrical performance has poor thermal performance and vice versa. However, if we look at the two-layer system (6 × 6_2x + 2y), the volumetric capacitance and power output values are the second highest in the selected electrodes. The volumetric capacitance of the two-layer system is 7.5 F cm^{-3}, and the power output is 1.52 × 10^{-8} W. Compared to the 12 × 12_1x electrode with the highest power output, only about 3.8% less power output is visible for the two-layer system. Therefore, the 12 × 12_1x system can be eliminated and replaced with the two-layer system. Nonetheless, compared to the vertical system (6 × 6_2Lz) with the highest capacitance, the two-layer system has a 44.8% lesser capacitance value. Therefore, we cannot completely eliminate the vertical system, regardless of its poor thermal performance. Vertically stacked CNT structures can be used if electrical performance is the only requirement. However, before drawing conclusions, other factors, such as the structural balance, production, and scalability of the electrode structure, must also be taken into account.

Manufacturing vertically aligned electrodes is challenging due to limited contact points with graphene and difficulty in maintaining the vertical alignment of CNTs. Structural stability is also a concern, and scaling up the thickness of the electrode is restricted by the length of the CNT. However, these issues do not apply to a two-layer electrode system that uses horizontal stacking of CNTs. This system offers higher structural stability, easier manufacturing, and the ability to adjust the pore size by controlling the distance between CNTs.

https://doi.org/10.1021/acs.jpcc.3c07299
J. Phys. Chem. C 2024, 128, 2190−2204

Considering these factors, the two-layer (multilayer) electrode system is the optimal structure with better electrical and thermal performances. Various techniques such as spin-casting,[58] self-assembly/solution phase processing,[29,59] and chemical vapor deposition methods[60,61] can be used to manufacture graphene/CNT composite electrodes. The multilayer structure can be obtained by functionalizing the surfaces of graphene and CNT with opposite charge groups, which enables electrostatic attraction between CNT and graphene.[62,63]

CONCLUSIONS

In summary, we have investigated the interfacial thermal transport in a graphene−IL supercapacitor, comparing constant charge and constant potential method MD simulations. To carry out the new constant potential simulations while enabling thermal transport, we use a novel, computationally efficient approach where the charge sites are on lattice points, but the atoms are allowed to move. Our results indicated that the constant potential and constant charge methods produce similar results for planar graphene electrodes because the IL structure is consistent between both methods. Furthermore, the ITR decreases as the electrode potential difference increases due to the increased density of ions close to the interface. Even though both methods give similar results in planar electrodes, the CCM is unsuitable for porous electrodes, and only the CPM can be used to understand the heat transfer mechanism during the charging/discharging process.

This study also aimed to identify the optimum electrode structure by modeling graphene/CNT composite electrodes and studying their electrical and thermal properties while varying the diameter, number, layers, and alignment of CNTs. It was observed that placing a CNT over the graphene layer led to a decrease in the ASA for ions compared with that of planar graphene. Vertically aligned CNT electrodes exhibited superior electrical performance, such as specific capacitance and energy density, while their thermal performance was inferior to that of horizontally aligned CNTs. Likewise, horizontally aligned CNTs with 12 × 12 chirality and two-layer-arranged electrode structures showed higher thermal performance. However, the single CNT with 12 × 12 chirality was not recommended due to poor electrical performance. Considering thermal and electrical aspects, the two-layer (multilayer) system is the optimal electrode structure. For the two-layer model ($6 \times 6_2x + 2y$), the volumetric capacitance increased by 108%, and the thermal power output increased by 10% compared to that of the planar graphene electrode. In future work, we will model different ILs at various concentrations using all-atom models to understand the nanoscale mechanisms more deeply. The multilayer electrode structure will also be further optimized with separately tuned pores for the cathode and anode, depending on the size of the anions and cations.

ASSOCIATED CONTENT

Supporting Information

The Supporting Information is available free of charge at https://pubs.acs.org/doi/10.1021/acs.jpcc.3c07299.

Comparison of ITR for different systems, normalized slab mass for different potential differences, different models of CNT/graphene composite electrodes, density profiles showing the selective ion entry, and VDOS of the IL and electrodes (PDF)

AUTHOR INFORMATION

Corresponding Authors

Sobin Alosious − *Australian Institute of Bioengineering and Nanotechnology, The University of Queensland, Brisbane, Queensland 4072, Australia;* orcid.org/0000-0003-3579-4747; Email: s.alosious@uq.edu.au

Debra J. Searles − *Australian Institute of Bioengineering and Nanotechnology, The University of Queensland, Brisbane, Queensland 4072, Australia; School of Chemistry and Molecular Biosciences, The University of Queensland, Brisbane, Queensland 4072, Australia;* orcid.org/0000-0003-1346-8318; Email: d.bernhardt@uq.edu.au

Author

Shern R. Tee − *School of Environment and Science, Griffith University, Nathan, Queensland 4111, Australia;* orcid.org/0000-0003-2701-005X

Complete contact information is available at: https://pubs.acs.org/10.1021/acs.jpcc.3c07299

Notes

The authors declare no competing financial interest.

ACKNOWLEDGMENTS

The authors thank the Australian Research Council for its support for this project through the Discovery program (FL190100080). We extend our thanks to the members of the Bernhardt group for their feedback and suggestions. This work was supported by resources provided by the Pawsey Supercomputing Research Centre with funding from the Australian Government and the Government of Western Australia and with the assistance of resources and services from the National Computational Infrastructure (NCI), which is supported by the Australian Government. We also wish to acknowledge The University of Queensland's Research Computing Centre (RCC) and Queensland Cyber Infrastructure Foundation (QCIF) for its support in this research.

REFERENCES

(1) Jaafar, A.; Sareni, B.; Roboam, X.; Thiounn-Guermeur, M. Sizing of a hybrid locomotive based on accumulators and ultracapacitors. *2010 IEEE Vehicle Power and Propulsion Conference*, 2010; pp 1−6.

(2) He, Y.; Wang, Z.; Zhang, Y. The design, test and application on the satellite separation system of space power supply based on graphene supercapacitors. *Acta Astronaut.* **2021**, *186*, 259−268.

(3) Şahin, M. E.; Blaabjerg, F. A hybrid PV-battery/supercapacitor system and a basic active power control proposal in MATLAB/Simulink. *Electronics* **2020**, *9*, 129.

(4) Farhadi, M.; Mohammed, O. A. Real-time operation and harmonic analysis of isolated and non-isolated hybrid DC microgrid. *IEEE Trans. Ind. Appl.* **2014**, *50*, 2900−2909.

(5) Xiong, G.; Kundu, A.; Fisher, T. S. *Thermal effects in supercapacitors*; Springer, 2015.

(6) Niu, J.; Conway, B. E.; Pell, W. G. Comparative studies of self-discharge by potential decay and float-current measurements at C double-layer capacitor and battery electrodes. *J. Power Sources* **2004**, *135*, 332−343.

(7) Kötz, R.; Ruch, P.; Cericola, D. Aging and failure mode of electrochemical double layer capacitors during accelerated constant load tests. *J. Power Sources* **2010**, *195*, 923−928.

(8) Xiong, G.; Meng, C.; Reifenberger, R. G.; Irazoqui, P. P.; Fisher, T. S. A review of graphene-based electrochemical microsupercapacitors. *Electroanalysis* **2014**, *26*, 30−51.
(9) Xiong, G.; Meng, C.; Reifenberger, R. G.; Irazoqui, P. P.; Fisher, T. S. Graphitic petal micro-supercapacitor electrodes for ultra-high power density. *Energy Technol.* **2014**, *2*, 897−905.
(10) Hijazi, A.; Kreczanik, P.; Bideaux, E.; Venet, P.; Clerc, G.; Di Loreto, M. Thermal network model of supercapacitors stack. *IEEE Trans. Ind. Electron.* **2012**, *59*, 979−987.
(11) Guillemet, P.; Scudeller, Y.; Brousse, T. Multi-level reduced-order thermal modeling of electrochemical capacitors. *J. Power Sources* **2006**, *157*, 630−640.
(12) Rashidi, S.; Karimi, N.; Sunden, B.; Kim, K. C.; Olabi, A. G.; Mahian, O. Progress and challenges on the thermal management of electrochemical energy conversion and storage technologies: Fuel cells, electrolysers, and supercapacitors. *Prog. Energy Combust. Sci.* **2022**, *88*, 100966.
(13) Pollack, G. L. Kapitza resistance. *Rev. Mod. Phys.* **1969**, *41*, 48−81.
(14) Anandakrishnan, A.; Ramos-Alvarado, B.; Kannam, S. K.; Sathian, S. P. Effects of interfacial molecular mobility on thermal boundary conductance at solid−liquid interface. *J. Chem. Phys.* **2023**, *158*, 094710.
(15) Rabani, R.; Saidi, M. H.; Rajabpour, A.; Joly, L.; Merabia, S. Enhanced heat flow between charged nanoparticles and an aqueous electrolyte. *Langmuir* **2023**, *39*, 15222−15230.
(16) Alosious, S.; Kannam, S. K.; Sathian, S. P.; Todd, B. Kapitza resistance at water−graphene interfaces. *J. Chem. Phys.* **2020**, *152*, 224703.
(17) Alexeev, D.; Chen, J.; Walther, J. H.; Giapis, K. P.; Angelikopoulos, P.; Koumoutsakos, P. Kapitza resistance between few-layer graphene and water: Liquid layering effects. *Nano Lett.* **2015**, *15*, 5744−5749.
(18) Gonzalez-Valle, C. U.; Paniagua-Guerra, L. E.; Ramos-Alvarado, B. Implications of the interface modeling approach on the heat transfer across graphite−water interfaces. *J. Phys. Chem. C* **2019**, *123*, 22311−22323.
(19) Qian, C.; Ding, B.; Wu, Z.; Ding, W.; Huo, F.; He, H.; Wei, N.; Wang, Y.; Zhang, X. Ultralow thermal resistance across the solid−ionic liquid interface caused by the charge-induced ordered ionic layer. *Ind. Eng. Chem. Res.* **2019**, *58*, 20109−20115.
(20) Qian, C.; Wang, Y.; He, H.; Huo, F.; Wei, N.; Zhang, S. Lower limit of interfacial thermal resistance across the interface between an imidazolium ionic liquid and solid surface. *J. Phys. Chem. C* **2018**, *122*, 22194−22200.
(21) Frackowiak, E.; Abbas, Q.; Béguin, F. Carbon/carbon supercapacitors. *J. Energy Chem.* **2013**, *22*, 226−240.
(22) Barbieri, O.; Hahn, M.; Herzog, A.; Kötz, R. Capacitance limits of high surface area activated carbons for double layer capacitors. *Carbon* **2005**, *43*, 1303−1310.
(23) Chmiola, J.; Yushin, G.; Gogotsi, Y.; Portet, C.; Simon, P.; Taberna, P.-L. Anomalous increase in carbon capacitance at pore sizes less than 1 nanometer. *Science* **2006**, *313*, 1760−1763.
(24) Ma, Z.; Kyotani, T.; Tomita, A. Preparation of a high surface area microporous carbon having the structural regularity of Y zeolite. *Chem. Commun.* **2000**, 2365−2366.
(25) García-Gómez, A.; Moreno-Fernández, G.; Lobato, B.; Centeno, T. A. Constant capacitance in nanopores of carbon monoliths. *Phys. Chem. Chem. Phys.* **2015**, *17*, 15687−15690.
(26) Niu, C.; Sichel, E. K.; Hoch, R.; Moy, D.; Tennent, H. High power electrochemical capacitors based on carbon nanotube electrodes. *Appl. Phys. Lett.* **1997**, *70*, 1480−1482.
(27) Péan, C.; Merlet, C.; Rotenberg, B.; Madden, P. A.; Taberna, P.-L.; Daffos, B.; Salanne, M.; Simon, P. On the dynamics of charging in nanoporous carbon-based supercapacitors. *ACS Nano* **2014**, *8*, 1576−1583.
(28) Maji, S.; Chaudhary, R.; Shrestha, R. G.; Shrestha, R. L.; Demir, B.; Searles, D. J.; Hill, J. P.; Yamauchi, Y.; Ariga, K.; Shrestha, L. K. High-performance supercapacitor materials based on hierarchically porous carbons derived from *Artocarpus heterophyllus* seed. *ACS Appl. Energy Mater.* **2021**, *4*, 12257−12266.
(29) Cheng, Q.; Tang, J.; Ma, J.; Zhang, H.; Shinya, N.; Qin, L.-C. Graphene and carbon nanotube composite electrodes for supercapacitors with ultra-high energy density. *Phys. Chem. Chem. Phys.* **2011**, *13*, 17615−17624.
(30) Yang, S.-Y.; Chang, K.-H.; Tien, H.-W.; Lee, Y.-F.; Li, S.-M.; Wang, Y.-S.; Wang, J.-Y.; Ma, C.-C. M.; Hu, C.-C. Design and tailoring of a hierarchical graphene-carbon nanotube architecture for supercapacitors. *J. Mater. Chem.* **2011**, *21*, 2374−2380.
(31) Buglione, L.; Pumera, M. Graphene/carbon nanotube composites not exhibiting synergic effect for supercapacitors: The resulting capacitance being average of capacitance of individual components. *Electrochem. Commun.* **2012**, *17*, 45−47.
(32) McDaniel, J. G. Capacitance of carbon nanotube/graphene composite electrodes with $[BMIM^+]$ $[BF_4^-]$/acetonitrile: Fixed voltage molecular dynamics simulations. *J. Phys. Chem. C* **2022**, *126*, 5822−5837.
(33) Merlet, C.; Péan, C.; Rotenberg, B.; Madden, P. A.; Simon, P.; Salanne, M. Simulating supercapacitors: Can we model electrodes as constant charge surfaces? *J. Phys. Chem. Lett.* **2013**, *4*, 264−268.
(34) Wang, Z.; Yang, Y.; Olmsted, D. L.; Asta, M.; Laird, B. B. Evaluation of the constant potential method in simulating electric double-layer capacitors. *J. Chem. Phys.* **2014**, *141*, 184102.
(35) Siepmann, J. I.; Sprik, M. Influence of surface topology and electrostatic potential on water/electrode systems. *J. Chem. Phys.* **1995**, *102*, 511−524.
(36) Scalfi, L.; Limmer, D. T.; Coretti, A.; Bonella, S.; Madden, P. A.; Salanne, M.; Rotenberg, B. Charge fluctuations from molecular simulations in the constant-potential ensemble. *Phys. Chem. Chem. Phys.* **2020**, *22*, 10480−10489.
(37) Pireddu, G.; Rotenberg, B. Frequency-dependent impedance of nanocapacitors from electrode charge fluctuations as a probe of electrolyte dynamics. *Phys. Rev. Lett.* **2023**, *130*, 098001.
(38) Lindsay, L.; Broido, D. Optimized Tersoff and Brenner empirical potential parameters for lattice dynamics and phonon thermal transport in carbon nanotubes and graphene. *Phys. Rev. B: Condens. Matter Mater. Phys.* **2010**, *81*, 205441.
(39) Tee, S. R.; Searles, D. J. Fully periodic, computationally efficient constant potential molecular dynamics simulations of ionic liquid supercapacitors. *J. Chem. Phys.* **2022**, *156*, 184101.
(40) Slack, G. A. Anisotropic thermal conductivity of pyrolytic graphite. *Phys. Rev.* **1962**, *127*, 694−701.
(41) Roy, D.; Maroncelli, M. An improved four-site ionic liquid model. *J. Phys. Chem. B* **2010**, *114*, 12629−12631.
(42) Ciccotti, G.; Ferrario, M.; Ryckaert, J.-P. Molecular dynamics of rigid systems in cartesian coordinates A general formulation. *Mol. Phys.* **1982**, *47*, 1253−1264.
(43) McDaniel, J. G. Polarization effects in binary $[BMIM^+]$ $[BF_4^-]$/1,2-dichloroethane, acetone, acetonitrile, and water electrolytes. *J. Phys. Chem. B* **2018**, *122*, 4345−4355.
(44) Son, C. Y.; McDaniel, J. G.; Schmidt, J. R.; Cui, Q.; Yethiraj, A. First-principles united atom force field for the ionic liquid $BMIM^+BF_4^-$: An alternative to charge scaling. *J. Phys. Chem. B* **2016**, *120*, 3560−3568.
(45) Bedrov, D.; Piquemal, J.-P.; Borodin, O.; MacKerell, A. D. J.; Roux, B.; Schröder, C. Molecular dynamics simulations of ionic liquids and electrolytes using polarizable force fields. *Chem. Rev.* **2019**, *119*, 7940−7995.
(46) Merlet, C.; Salanne, M.; Rotenberg, B.; Madden, P. A. Imidazolium ionic liquid interfaces with vapor and graphite: interfacial tension and capacitance from coarse-grained molecular simulations. *J. Phys. Chem. C* **2011**, *115*, 16613−16618.
(47) Hockney, R. W.; Eastwood, J. W. *Computer simulation using particles*; CRC Press, 2021.
(48) Yeh, I.-C.; Berkowitz, M. L. Ewald summation for systems with slab geometry. *J. Chem. Phys.* **1999**, *111*, 3155−3162.
(49) Thompson, A. P.; Aktulga, H. M.; Berger, R.; Bolintineanu, D. S.; Brown, W. M.; Crozier, P. S.; in 't Veld, P. J.; Kohlmeyer, A.;

https://doi.org/10.1021/acs.jpcc.3c07299
J. Phys. Chem. C 2024, 128, 2190−2204

Moore, S. G.; Nguyen, T. D.; Shan, R.; Stevens, M. J.; Tranchida, J.; Trott, C.; Plimpton, S. J. LAMMPS - a flexible simulation tool for particle-based materials modeling at the atomic, meso, and continuum scales. *Comp. Phys. Comm.* **2022**, *271*, 108171.
(50) Humphrey, W.; Dalke, A.; Schulten, K. VMD: Visual molecular dynamics. *J. Mol. Graphics* **1996**, *14*, 33−38.
(51) Stukowski, A. Visualization and analysis of atomistic simulation data with OVITO−the Open Visualization Tool. *Modell. Simul. Mater. Sci. Eng.* **2010**, *18*, 015012.
(52) Grest, G. S.; Kremer, K. Molecular dynamics simulation for polymers in the presence of a heat bath. *Phys. Rev. A* **1986**, *33*, 3628−3631.
(53) Alosious, S.; Kannam, S. K.; Sathian, S. P.; Todd, B. Nanoconfinement effects on the Kapitza resistance at water−CNT interfaces. *Langmuir* **2021**, *37*, 2355−2361.
(54) Shrake, A.; Rupley, J. A. Environment and exposure to solvent of protein atoms. Lysozyme and insulin. *J. Mol. Biol.* **1973**, *79*, 351−371.
(55) Saffarimiandoab, F.; Sabetvand, R.; Zhang, X. Molecular insights into capacitive deionization mechanisms inside hydrophobic and hydrophilic carbon nanotube channel electrodes. *J. Mater. Chem. A* **2022**, *10*, 23332−23340.
(56) Alosious, S.; Kannam, S. K.; Sathian, S. P.; Todd, B. Prediction of Kapitza resistance at fluid-solid interfaces. *J. Chem. Phys.* **2019**, *151*, 194502.
(57) Alosious, S.; Kannam, S. K.; Sathian, S. P.; Todd, B. Effects of electrostatic interactions on Kapitza resistance in hexagonal boron nitride−water interfaces. *Langmuir* **2022**, *38*, 8783−8793.
(58) Shakir, I. High energy density based flexible electrochemical supercapacitors from layer-by-layer assembled multiwall carbon nanotubes and graphene. *Electrochim. Acta* **2014**, *129*, 396−400.
(59) Qiu, L.; Yang, X.; Gou, X.; Yang, W.; Ma, Z.-F.; Wallace, G. G.; Li, D. Dispersing carbon nanotubes with graphene oxide in water and synergistic effects between graphene derivatives. *Chem.—Eur. J.* **2010**, *16*, 10653−10658.
(60) Fan, Z.; Yan, J.; Zhi, L.; Zhang, Q.; Wei, T.; Feng, J.; Zhang, M.; Qian, W.; Wei, F. A three-dimensional carbon nanotube/graphene sandwich and its application as electrode in supercapacitors. *Adv. Mater.* **2010**, *22*, 3723−3728.
(61) Niu, Z.; Zhang, Y.; Zhang, Y.; Lu, X.; Liu, J. Enhanced electrochemical performance of three-dimensional graphene/carbon nanotube composite for supercapacitor application. *J. Alloys Compd.* **2020**, *820*, 153114.
(62) Yu, D.; Dai, L. Self-assembled graphene/carbon nanotube hybrid films for supercapacitors. *J. Phys. Chem. Lett.* **2010**, *1*, 467−470.
(63) Byon, H. R.; Lee, S. W.; Chen, S.; Hammond, P. T.; Shao-Horn, Y. Thin films of carbon nanotubes and chemically reduced graphenes for electrochemical micro-capacitors. *Carbon* **2011**, *49*, 457−467.



https://doi.org/10.1021/acs.jpcc.3c07299
J. Phys. Chem. C 2024, 128, 2190−2204